

# Simultaneous determination of benzene, toluene and xylene (BTX) by Au nanoparticles (AuNP) anchored in reduced graphene oxide electrode

Ismael Carlos Braga Alves<sup>1</sup> | José Ribamar Nascimento dos Santos<sup>1</sup> |  
Edmar Pereira Marques<sup>1</sup>  | Lorena Carvalho Martiniano de Azevedo<sup>1</sup> |  
Maísa Azevedo Beluomini<sup>2</sup> | Nelson Ramos Stradiotto<sup>2</sup> |  
Aldaléa Lopes Brandes Marques<sup>1</sup>

<sup>1</sup>NEPE (LPQA & LAPQAP), PPG-BIONORTE, Federal University of Maranhão (UFMA), São Luís, MA, Brazil

<sup>2</sup>Institute of Chemistry, São Paulo State University (UNESP), Araraquara, SP, Brazil

## Correspondence

Ismael Carlos Braga Alves and Aldaléa Lopes Brandes Marques, NEPE (LPQA & LAPQAP), PPG-BIONORTE, Federal University of Maranhão (UFMA), São Luís, 65085-580 MA, Brazil.

Email: [ismael.cba@ufma.br](mailto:ismael.cba@ufma.br) and [aldalea.ufma@gmail.com](mailto:aldalea.ufma@gmail.com)

## Funding information

CAPES-PROCAD AM, Grant/Award Number: SCBA: 88887.200615/2018-00]; CNPq, Grant/Award Number: 310664/2017-9; FAPEMA, Grant/Award Number: 01136/17; ANP, Grant/Award Number: 1.028/2021, 2.460/22; FAPESP, Grant/Award Number: 2018/12131-6, 2017/22401-8

## Abstract

This work reports the development of an electrochemical sensor for the simultaneous determination of benzene, toluene and xylene (BTX). The sensor was prepared by coating the glassy carbon electrode (GCE) with reduced graphene oxide (RGO) film, decorated with gold nanoparticles (AuNP), by electrodeposition. Surface modification with AuNP/RGO-GCE favored the electron transfer process and increased the active area, providing greater sensitivity for the sensor. The AuNP/RGO-GCE sensor was characterized by cyclic voltammetry (CV), electrochemical impedance spectroscopy (EIS) and scanning electron microscope (SEM). Quantitative analyses of BTX were carried out using the differential pulse voltammetry (DPV) technique, after optimization of the parameters that influence the sensor performance. The sensor showed a linear response in the 30–240  $\mu\text{M}$  concentration range, with a detection limit range of 1.8–2.2  $\mu\text{M}$ , 2.2–2.7  $\mu\text{M}$ , and 2.0–2.6  $\mu\text{M}$ , and quantification limit range of 6.2–7.3  $\mu\text{M}$ , 7.2–8.9  $\mu\text{M}$ , and 6.6–8.8  $\mu\text{M}$ , respectively for B, T and X. In addition to the satisfactory repeatability and stability, in the determination of BTX, the method still showed good selectivity even in the presence of molecules with similar chemical structure, such as: catechol, *p*-benzoquinone, resorcinol, ethanol, pyrene and in the presence of  $\text{K}^+$ ,  $\text{Mg}^{2+}$  and  $\text{Pb}^{2+}$  ions. The device was successfully applied for the determination of the analytes (BTX) in water samples from fuel station separator boxes, where recovery rates close to 100% (97.8% to 103.1%) were obtained. The results obtained suggest that the AuNP/RGO-GCE sensor has strong potential for detecting BTX in wastewater discharge from industrial processes.

## KEYWORDS

Au nanoparticles, BTX, electrochemical determination, reduced graphene oxide

## 1 | INTRODUCTION

Contamination of soil, water and air by volatile organic compounds is largely due to petroleum derivatives [1]. Among the aromatic hydrocarbons, BTX stand out as contaminants [2] and are substances that cause great concern due to their harmful effects on human health [3, 4]. B is considered the most harmful among the BTX, considered a human carcinogen, in which it favors the risk of contracting leukemia and lymphoma [4, 5].

In Brazil, the maximum values established by the National Council for the Environment (CONAMA) for releasing effluents into water bodies are  $1.2 \text{ mgL}^{-1}$  (B),  $1.2 \text{ mgL}^{-1}$  (T) and  $1.6 \text{ mgL}^{-1}$  (X) [6]. Considering the management and disposal of process or production water on offshore oil and natural gas platforms, Brazilian legislation establishes a monthly arithmetic average concentration of  $29 \text{ mgL}^{-1}$ , with a maximum value of  $42 \text{ mgL}^{-1}$  of grease and oil [7]. In other countries, the established limits of total oils and greases are between  $15 \text{ mgL}^{-1}$  and  $50 \text{ mgL}^{-1}$ , as an example of the United States, where the established limits are  $29 \text{ mgL}^{-1}$  [8, 9], and the United Kingdom that adopts a monthly limit of  $30 \text{ mgL}^{-1}$  [10].

Different methods have been studied for the simultaneous determination of BTX, such as chromatographic [11] and spectroscopic techniques [5, 12, 13], Raman [14] and attenuated total reflection mid-infrared spectroscopy [5, 12]. Chromatographic techniques, although efficient, have some operational limitations, such as the high cost and the need specialized technicians, in addition to the use of bulky instrumentation, which makes monitoring in the field difficult. Electrochemical sensors have high sensitivity, high selectivity, high stability and good reproducibility [15]. Different studies using metallic oxides such as  $\text{TiO}_2$ ,  $\text{Co}_3\text{O}_4$ ,  $\text{WO}_3$ ,  $\text{ZnO}$ ,  $\text{Cr}_2\text{O}_3$ ,  $\text{SnO}_2$ , among others, have been used as sensors for the individual or simultaneous determination of BTX [16–22]. Electroanalytical techniques are considered simple and easy to operate, resulting in time and cost savings compared to chromatographic and spectroscopic techniques. Carrying out extensive bibliographical research, in the Scopus and Web of Science databases, for simultaneous electrochemical determination of BTX, only the work using cathodically treated boron-doped diamond electrode was found [23].

Researchers have improved the sensitivity and selectivity of electrochemical sensors by modifying them with different materials [24–27]. Graphene, amidst the materials studied, has gained considerable relevance due to its durability, flexibility, lightness, and properties such as excellent electrical conductivity and high capacitance [28]. Graphene oxide (GO) and reduced graphene oxide

(RGO) come from graphene, GO being the oxidized form and RGO the reduced form. RGO can be obtained by chemical, thermoelectrochemical or photothermal reduction [29, 30]. Among these methods, electrochemical reduction has been used due to its practicality in obtaining the RGO, applying electrode potential to control the degree of reduction of the RGO [31, 32]. Due to its excellent properties such as conductivity, thermal and chemical stability, in addition to its large specific surface area and high mechanical properties, RGO has been widely used in several studies, including as sensors [33, 34].

The metallic nanoparticles of noble metals have excellent electrochemical performance and excellent electrical conductivity, being considered ideal for applications in electrochemical sensors [35], being able to help in high electron transfer caused due to small size and large surface area to volume ratio [36, 37]. AuNP has been widely used to increase conductivity in addition to accelerating charge transfer [38]. These factors corroborate to provide a better electrochemical response for the sensor in terms of current, making them a considerably ideal material for different applications such as chemical and biological sensors [38, 39].

In this study, an electrochemical sensor was built based on RGO-GCE modified with AuNP obtained by electrodeposition, thus ensuring the control of the sensor thickness, its reproducibility and stability, to concurrently quantify BTX in wastewater, from the separator box of the fuel station. The presence of the nanomaterials AuNP and RGO in the modified surface showed an increase in the electrode active surface and electrical conductivity, leading to an improved performance of the electrochemical sensor, providing greater sensitivity for the sensor.

## 2. | EXPERIMENTAL

### 2.1 | Reagents and apparatus

Potassium ferricyanide ( $\text{K}_3[\text{Fe}(\text{CN})_6]$ , purity: 99%), potassium chloride, sodium sulfate, and acetonitrile (purity: 99.8%), benzene (purity: 99.8%), pyrocatechol (purity:  $\geq 99.5\%$ ), *p*-benzoquinone (purity: 98%), pyrene (purity: 98%), ethanol (purity:  $\geq 99.8\%$ ), chloroauric acid and graphene oxide suspension (GO, purity:  $> 95\%$ ) were purchased from Sigma-Aldrich. Sulfuric acid (purity: 95–97% Merck, Germany), toluene (purity:  $> 99.9\%$ , Synth, Brazil), xylene (purity:  $> 98.5\%$ , Neon, Brazil), resorcinol (purity:  $> 98\%$ , Synth, Brazil), and sodium hydroxide (purity:  $\geq 97\%$ , Neon, Brazil) were also purchased. Lead, potassium, and magnesium Standard Solution (at a

concentration of  $1000 \text{ mg L}^{-1}$  in 2% to 5%  $\text{HNO}_3$ , 125 mL package, uncertainty  $\simeq 0.2\%$ ) were purchased from Group Chemical Brazil. The 10 mM stock solution of benzene, toluene and xylene were prepared in ultrapure water with 20% (v:v) acetonitrile. Millipore ultrapure water ( $R \geq 18.2 \text{ M}\Omega \text{ cm}$ ) was used in all experiments.

Electrochemical measurements were performed using Metrohm-Autolab model PGSTAT 302 potentiostat coupled to a microcomputer controlled by NOVA 2.1 software. A conventional three-electrode cell was used: working electrode (GCE  $A_{\text{geom}} = 0.07 \text{ cm}^2$ ), auxiliary (platinum wire) and reference Ag/AgCl (KCl 3.0 M). A magnetic stirrer was used for the convective transport when necessary. All experiments were carried out at room temperature ( $\sim 25^\circ\text{C}$ ). The morphological characterization of the materials was carried out through scanning electron microscopy (SEM) obtained from a scanning electron microscope (Model 7500F, JEOL).

## 2.2 | Preparation of RGO-GCE

Before deposition process the GCE was polished with  $0.3 \mu\text{m}$  alumina powder on a felt and electrochemically subjected to successive potential scans into a solution containing  $\text{H}_2\text{SO}_4$  (0.50 M) in the  $-0.50 \text{ V}$  to  $+1.5 \text{ V}$  potential range, at  $0.020 \text{ Vs}^{-1}$ , to obtain a cyclic voltammogram showing characteristics of a clean GCE.

The deposition of the reduced graphene oxide (RGO) film occurred through a typical process reported in the literature [39, 40]. The RGO film was prepared by electrodeposition of a suspension of graphene oxide (Sigma-Aldrich-USA), onto a bare surface of GCE based on previous work [39]. Parameters such as graphene oxide suspension concentration, applied potential and deposition time were optimized according to a previous work [39], where  $0.50 \text{ mg mL}^{-1}$  of graphene oxide suspension in 0.10 M  $\text{Na}_2\text{SO}_4$  was electrodeposited at a potential of  $-1.5 \text{ V}$  for 500 s. After modification, the electrode was dried at room temperature.

## 2.3 | Preparation of AuNP/RGO-GCE

Gold nanoparticles (AuNP) were electrodeposited on the RGO-GCE surface by chronoamperometry, applying a potential of  $+0.4 \text{ V}$  (vs. Ag/AgCl) for 600 s in a 0.50 M  $\text{H}_2\text{SO}_4$  solution containing  $600 \mu\text{M}$   $\text{HAuCl}_4$ . The film was obtained in 0.50 M NaOH by cyclic voltammetry with 30 cycles in the potential range ( $-0.40 \text{ V}$  to  $+0.50 \text{ V}$  vs. Ag/AgCl) with a scan rate of  $0.050 \text{ Vs}^{-1}$  (Figure S1). The entire process of optimization and characterization of the film was carried out in previous work [39].

## 2.4 | Electroanalytical measurements

The electrochemical characterization of AuNP/RGO-GCE was performed using CV and EIS techniques. CVs were recorded at potentials ranging from 0.0 V to 1.9 V with a scan rate of  $0.050 \text{ Vs}^{-1}$ . The EIS measurements, carried out in a Faraday cage, were recorded at a potential of 0.22 V (vs. Ag/AgCl), in the frequency range of 0.10 Hz to 100 kHz.

For the electroanalytical application, AuNP/RGO-GCE electrode was evaluated by Differential Pulse Voltammetry (DPV) in the potential range from 1.0 V to 1.9 V. Firstly, the parameters were optimized varying amplitude, pulse time and step potential. All these measurements were carried out in the support electrolyte  $\text{H}_2\text{SO}_4$  0.50 M. The B was used as a model to optimize the DPV parameters. Figure S2 (A and B) shows the pulse amplitude tests in the range of 0.010 V–0.10 V, and Figure S2C shows the pulse time from 0.10 s to 0.70 s. The potential increment, in the 0.0010 V–0.0070 V potential range is presented in Figure S2D. Based on these experiments, the following parameters were selected for future measurements: amplitude 0.060 V, pulse time 0.60 s, step potential 0.0050 V, and the scan rate resulting from the influence of the optimized parameters was  $0.084 \text{ Vs}^{-1}$ .

Calibration curves with the AuNP/RGO-GCE sensor were obtained using the optimized DPV parameters. The values referring to the limit of detection (LOD) and limit of quantification (LOQ), as well as the standard deviation of the intercept ( $SD$ ), and the slope of the calibration curves ( $S$ ) were determined using the classical statistical approach based on the IUPAC definitions and ACS [41] that shows that the limits =  $k \times (SD/S)$  with factor  $k = 3$  and 10, respectively.

## 2.5 | Real sample preparation and quantification method

The wastewater sample was collected at a gas station located in the city of São Luís, State of Maranhão, Brazil. The sample was collected in an amber glass flask previously cleaned with Extran<sup>®</sup> solution and dried in an oven at  $100^\circ\text{C}$  for 24 h. During collection, the amber glass vial containing the sample was kept in an ice bath and then taken to the laboratory and stored at controlled temperature ( $\sim 4.0^\circ\text{C}$ ) for a maximum period of 20 days. The sample was diluted with 0.50 M  $\text{H}_2\text{SO}_4$  solution, in a proportion of 1:1 (v:v) to perform electrochemical measurements by differential pulse voltammetry (DPV). The BTX concentrations in the sample were determined by the standard addition method. To perform the recovery

analysis, known amounts of BTX were added to the original sample, using the methodology proposed by Burns, Danzer and Townshend [42].

### 3 | RESULTS AND DISCUSSION

#### 3.1 | Electrochemical and morphological characterization

For evaluate the electrochemical properties related to each modification, CV and EIS techniques were carried out using 5.0 mM  $[\text{Fe}(\text{CN})_6]^{3-/4-}$  in 0.1 M KCl as an electrolytic solution to monitor the change in electrochemical behavior during sensor formation. Typical redox peaks were recorded for the bare GCE according to Figure 1A (curve a). After modifying the GCE with RGO (curve b) there was an increase in peak current ( $\Delta I_p = 23.3 \mu\text{A}$ ), resulting from better electrical conductivity and high surface-to-volume ratio compared to graphene nanosheets. The addition of AuNP to the RGO-GCE electrode (curve c) resulted in an even greater increase in current ( $\Delta I_p = 46.1 \mu\text{A}$ ) in relation to the GCE. The justification for this increase in current response is attributed to gold nanoparticles, which contributed to enable the transfer of electrons by the electrochemical probe, consequently making the sensor more sensitive [43].

The electrochemical active area for AuNP/RGO-GCE was calculated by CV in the presence of 5.0 mM  $[\text{Fe}(\text{CN})_6]^{3-/4-}$  in 0.1 M KCl, at different scan rates (Figure S3) using the Randles-Sevcik equation Eq. (1) [44].

$$I_{ap} = 2.69 \times 10^5 n^{3/2} A D^{1/2} C \nu^{1/2} \quad (1)$$

where  $I_{ap}$  reflects peak redox currents,  $A$  is the electrode area,  $n$  is the electron transfer number ( $n = 1$ ),  $D$  is the diffusion coefficient ( $7.6 \mu\text{cm}^2\text{s}^{-1}$ ),  $C$  is the concentration of  $[\text{Fe}(\text{CN})_6]^{3-/4-}$  ( $\text{molcm}^{-3}$ ) and  $\nu$  is scan rate ( $\text{Vs}^{-1}$ ). Area values of AuNP/RGO-GCE and bare GCE were estimated in  $0.082 \text{ cm}^2$  and  $0.065 \text{ cm}^2$ , respectively. These results demonstrate that the presence of the AuNP/RGO nanocomposite significantly improved the electrode area, consequently improving the electrochemical response of the target molecule on the electrode surface.

Furthermore, the surface roughness factor ( $R_f$ ), which has a marked effect on the manufacture of high-quality modified electrodes, was calculated as the ratio between the active area and the geometric area ( $0.07 \text{ cm}^2$ ). The  $R_f$  of AuNP/RGO-GCE was 1.2, which is greater than that of the GCE, which was 0.9. Thus,

AuNP/RGO-GCE presents itself as a promising electrode for electroanalysis applications.

EIS was used for the characterization of the electrochemical process on the electrode-electrolytic solution interface. The electron-transfer resistance was studied using a redox probe containing 5.0 mM  $\text{K}_3[\text{Fe}(\text{CN})_6]$  in 0.1 M KCl. The typical diagram of EIS includes a semi-circle and a straight line in the frequency range of 0.10 Hz to 100 kHz. The Nyquist diagram, in which the imaginary impedance  $Z''$  is plotted against the real number,  $Z'$ , is shown in Figure 1B. The standard Randle's equivalent circuit  $[R(Q[RW])]$  was used for fit modeling the EIS analysis for GCE and RGO-GCE, in which the first resistance is  $R_s$  and consist of the solution resistance.  $Q$  represents the constant phase element (CPE), which is identified as pure capacitor and is related to the double layer capacitance, and the second  $R$  represent the charge-transfer resistance,  $R_{ct}$ , and  $W$  the Warburg impedance. The capacitance arc in the high frequency region and a Warburg impedance line in the low frequency was observed for GCE and RGO-GCE, according to previous results reported in the literature [39, 45, 46]. The  $R_{ct}$  found for GCE was  $687.3 \Omega$ , while for RGO-GCE it was  $203.4 \Omega$ , showing that the electron transfer resistance on the electrode modified with RGO was approximately 3.3 times lower. For AuNP/RGO-GCE, an  $R_{ct}$  of  $126.7 \Omega$  was obtained, indicating that the modification with AuNP in RGO-GCE can further facilitate the electron transfer. Thus, the results obtained show that the modification of the electrode with RGO and AuNP was successfully performed, in addition to improving the electron transfer process.

The surface morphological analysis was performed by SEM. Figure 2 shows surface morphologies of GCE, RGO-GCE and AuNP/RGO-GCE using SEM. In Figure 2A have the bare GCE image. Figure 2B shows the image of a uniform electrodeposition of graphene nanosheets with a distribution in the GCE. Figure 2C presents as AuNP are dispersed uniformly in the graphene nanosheets on the surface of the GCE. This indicates the success of deposition of gold nanoparticles on the RGO-GCE surface, with dimensions of  $\sim 50 \text{ nm}$  in diameter. As can be seen in Figure 2C, AuNP/RGO-GCE was successfully built.

#### 3.2 | Electrochemical behavior of BTX on the sensor and proposed mechanism

The electrochemical behavior of BTX was investigated by CV (Figure 3), using the different electrodes (GCE, RGO-GCE and AuNP/RGO-GCE), in  $\text{H}_2\text{SO}_4$  0.50 M in

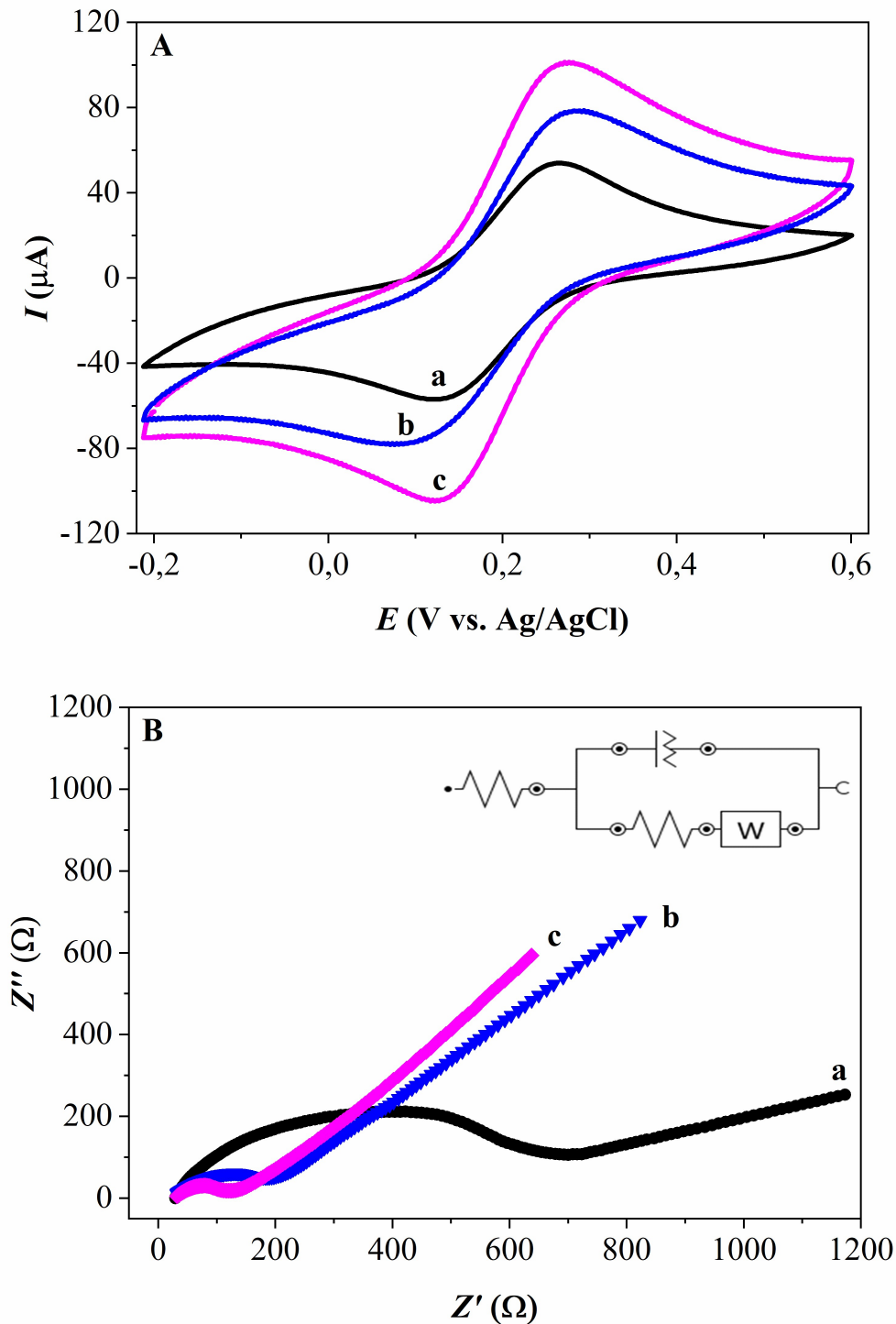


**FIGURE 1** (A) CVs behavior of (a) bare GCE, (b) RGO-GCE, (c) AuNP/RGO-GCE in the presence of 5.0 mM  $\text{K}_3[\text{Fe}(\text{CN})_6]$  in 0.10 M of KCl at a scan rate of  $0.10 \text{ V s}^{-1}$ . (B) Nyquist plot obtained for (a) GCE (b) RGO-GCE and (c) AuNP/RGO-GCE in the frequency range of 0.10 Hz – 100 kHz.

the potential range of 0.0 V–2.0 V, with a scan rate of  $0.050 \text{ V s}^{-1}$ , in the presence of 1.0 mM of BTX.

BTX oxidation can occur through different processes, depending on the electrode [47–51]. In Figure 3A it is

possible to verify the response of the electrodes in the presence of B with oxidation potential of 1.76 V (AuNP/RGO-GCE), 1.77 V (RGO-GCE) and 1.81 V (GCE). As can be seen in Figure 3A, in terms of current, the

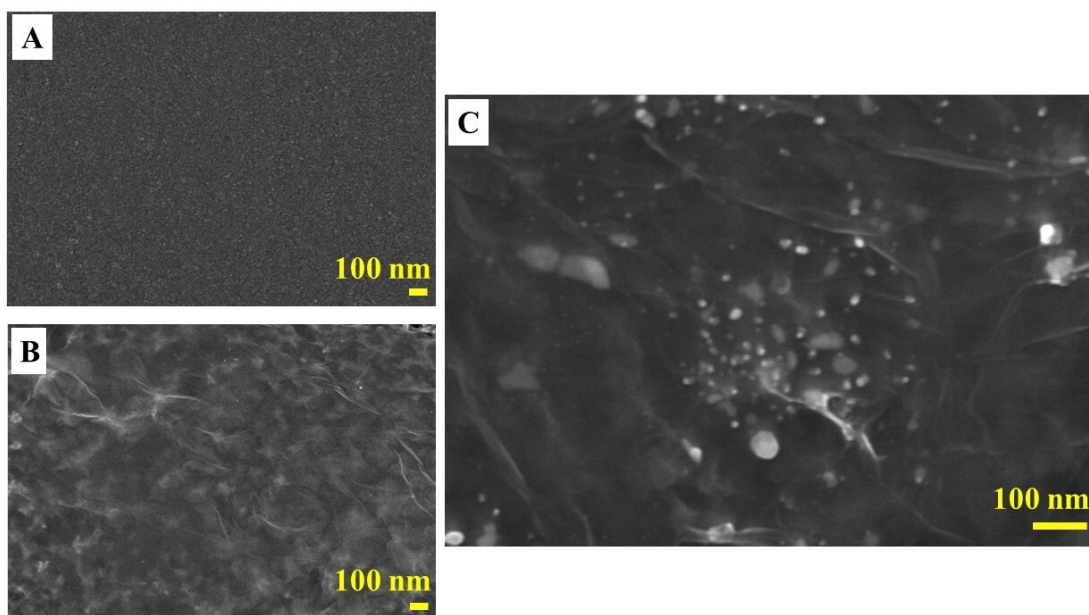


FIGURE 2 SEM images (A) bare GCE, (B) RGO-GCE and (C) AuNP/RGO-GCE.

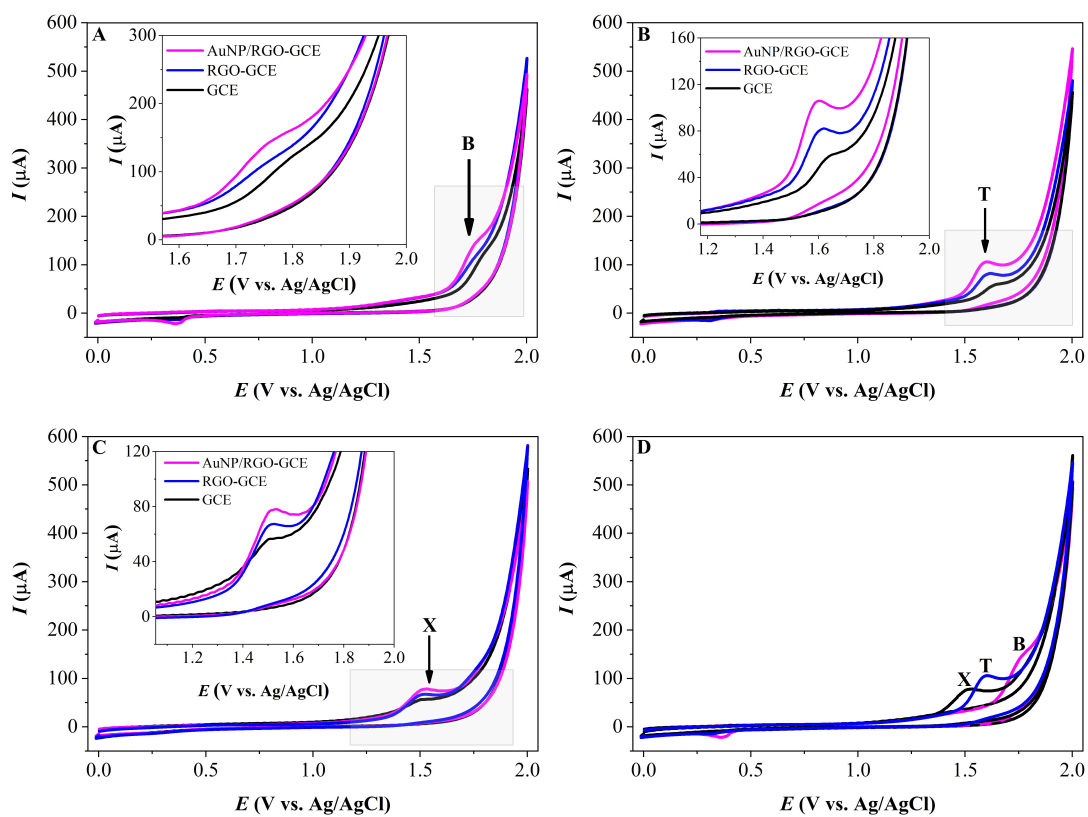


FIGURE 3 (A) CVs of electrodes GCE (black), RGO-GCE (blue) and AuNP/RGO-GCE (magenta) in the presence of 1 mM of B, (B) 1 mM of T and (C) 1 mM of X in 0.50 M  $\text{H}_2\text{SO}_4$ , scan rate =  $0.05 \text{ V s}^{-1}$ . (D) CVs of AuNP/RGO-GCE in the presence of 1.0 mM of X, T and B.

electrode AuNP/RGO-GCE presented a gain of  $\sim 44 \mu\text{A}$  when compared to the GCE and  $\sim 25 \mu\text{A}$  when compared to the RGO-GCE.

Second the literature [47, 48] B can be oxidized through the evolution of oxygen to benzoquinone presumably by active oxygen adsorbed on glassy carbon producing benzoquinone or quinone-like compounds from an aqueous B solution [48]. In this study, second Kim et al. [48] B oxidation reaction on carbon electrode could be in the oxygen evolution region.

On the other hand, another work [47] presents an electrochemical study of the B oxidation process in aqueous solution on boron-doped diamond electrode, through oxidation process, electrolysis and high-performance liquid chromatography experiments. In this study the complete electrochemical B degradation was performed in electrolysis experiments in 2.5 V for 5 h. The main products measured were hydroquinone, resorcinol, benzoquinone, catechol and phenol. These results [47, 48] corroborate with our results.

In the reverse scan, it is possible to observe the presence of the cathodic peak at the potential of  $\sim 0.37 \text{ V}$  for the three electrodes studied here.

This peak may be related to the presence of by-products formed through the electrochemical oxidation of B which react with radicals ( $\bullet\text{OH}$ ) on the electrode surface [47], such as: benzoquinone, hydroquinone [48], resorcinol, catechol, benzoquinone [52, 53], phenol, hexane and  $\text{CO}_2$  [54, 55]. Based in our recent work, we could consider that despite the possibility forming different by-products during the oxidation of B, the most likely is the formation of benzoquinone which is subsequently reduced to catechol taking into account the potential obtained at  $\sim 0.37 \text{ V}$  [47, 52, 56]. Further in the study of scan rate, it is possible to analyze the effect of the reversibility of catechol and quinone as they present a reversible quinonic form.

Figure 3B shows the electrochemical response of the electrodes to T, under the same conditions treated for B. The peak potential found for the T oxidation was 1.6 V, 1.63 V and 1.65 V for GCE, RGO-GCE and AuNP/RGO-GCE, respectively. The sensor AuNP/RGO-GCE presented a current delta of  $\sim 47.8 \mu\text{A}$  in relation to the GCE and of  $\sim 24.7 \mu\text{A}$  in relation to the RGO-GCE.

As can be observed the redox process of T oxidation is in the same region of B oxidation, i.e. in the oxygen evolution region. In the reverse scan, an anodic peak at  $\sim 0.31 \text{ V}$  was found, possibly related to the reduction of benzaldehyde produced in the oxidation of T, which is reduced, possibly forming benzyl alcohol, which can which can undergo oxidation to benzoic acid at  $\sim 0.35 \text{ V}$  [49, 50, 57].

Second the literature [49, 50] the electrochemical oxidation of T to benzaldehyde was observed at a carbon electrode via direct electron transfer [49]. In this study the electrochemical conditions were optimized by modifying cell configuration, electrolyte, solvent, electrode material, besides apply current for precise selectivity control, what revealed that the selectivity of the T oxidation reaction strongly depends on the applied current/potential and anode material. In optimized electrolysis conditions T was oxidized to benzaldehyde.

Another work [50] show the T oxidation to benzaldehyde on either a Pt/Ir or a mercury electrode by an electrochemical process involving  $\bullet\text{OH}$  radicals. In this study, in the presence of T the  $\bullet\text{OH}$  radicals oxidize the  $-\text{CH}_3$  group to  $-\text{CHO}$  with 100% selectivity. Second the authors, their results indicate that for the electrochemical systems studied no product other than benzaldehyde could be detected either with gas chromatographic or with mass spectrometry.

Figure 3C shows the CV for the electrodes in the presence of X, with peak potentials of 1.51 V (AuNP/RGO-GCE), 1.52 V (RGO-GCE) and 1.54 V (GCE). In terms of peak current, the modified sensor presented a current gain of  $\sim 23.1 \mu\text{A}$  when compared to the GCE and  $\sim 11.5 \mu\text{A}$  when compared to the RGO-GCE.

These results for X also show a redox behavior as the other aromatic compounds of BT, i.e., in the oxygen evolution region. Loyson et al. [51] studied the electrochemical oxidation of *p*-xylene (A) in methanol solutions using graphite electrodes in tetraethylammonium *p*-toluene sulphonate as supporting electrolyte [51]. The study showed that *p*-X is first oxidized to the intermediate 4-methylbenzyl methyl ether (B), which is then further oxidized to the corresponding acetal, 4-methyl benzaldehyde dimethyl acetal (C). The stepwise reaction ( $\text{A} \rightarrow \text{B} \rightarrow \text{C}$ ) is discussed, considering a parallel consecutive second order kinetics in which solvent participation assists in the electrochemical oxidation of the substrate, through free radical reactions.

Balaganesh et al. [58] showed the oxidation of *p*-xylene by electrolysis in an emulsion composed of a substrate containing chloroform, 2% aqueous sodium nitrate solution as mediator, and a catalytic amount of  $\text{H}_2\text{SO}_4$ , in which *p*-tolualdehyde was produced as a byproduct final.

In spite of usually, X oxidation is not studied in aqueous media, in this work carried out the experiment in aqueous acid solution and observed clearly the oxidation of the compound X, as showed in Figure 3C. In the reverse sweep, no faradaic current was observed in the studied range, demonstrating that X oxidation occurs irreversibly.

Due to the synergistic effect caused by AuNP and RGO on the GCE surface, the best conditions were

obtained in terms of current peak potential for the presentation of BTX using the AuNP/RGO-GCE sensor. As showed in Figure 3D the CV for the AuNP/RGO-GCE sensor in the presence of 1.0 mM of BTX, it is possible to clearly observe the positions of the peaks corresponding to each analyte, demonstrating that the electrode responds at distinct potentials for each of them BTX.

The effect of scan rate on the electrochemical behavior of BTX was analyzed by CV using BTX 1.0 mM in H<sub>2</sub>SO<sub>4</sub>. CVs were obtained at different scan rates ranging from 0.10 Vs<sup>-1</sup> to 0.50 Vs<sup>-1</sup> for B (Figure S4A), T (Figure S5A) and X (Figure S6A). Through the voltammograms, it was possible to obtain a linear relationship between log *I<sub>p</sub>* vs. log *v* for B (Figure S4B), T (Figure S5B) and X (Figure S6B). The obtained equations, in terms of linear relationships, were: log *I* = 0.7 log *v* - 2.7 (*R*<sup>2</sup> = 0.998); log *I* = 1.1 log *v* - 2.6 (*R*<sup>2</sup> = 0.997) and log *I* = 0.8 log *v* - 2.5 (*R*<sup>2</sup> = 0.997), respectively. According to the literature, a slope of log *I* vs. log *v* close to 0.50 can be attributed to the diffusion-controlled process, while a slope of 1.0 is associated with the adsorption process [59–61]. According to the obtained equations, a slope of 0.7 was obtained for B, which falls between 0.5 and 1.0, indicating that the oxidation of B was controlled by a mixed adsorption-diffusion process on the AuNP/RGO-GCE surface. This result is consistent with similar studies reported in previous literature [62].

In an evaluation about the adsorption of B (data not shown), it was observed that when exposed the electrode AuNP/RGO-GCE in a B aqueous acid solution (1 mM in H<sub>2</sub>SO<sub>4</sub> 0.5 M), and the electrode was transferred to an other media where there was only the supporting electrolyte no peak was observed for B. However, it is waited B is adsorbed on carbon electrode surfaces [63], but due to its volatility it doesn't stay on the electrode surface.

For T, an angular coefficient of 1.1 was obtained, which can be attributed to the adsorptive process [64]. For X, a value of 0.8 was obtained, similar to B, indicating a mixed process of adsorption-diffusion on the surface of AuNP/RGO-GCE [65]. In this case, the results show a behaviour more adsorptive for X.

Different of B, the same experiment to evaluate adsorption was carried out for B and X, showing that these two compounds were transferred attached on the electrode surface to another medium containing only the supporting electrolyte (data not shown). In these cyclic voltammetry experiments, characteristic peaks of T and X were observed, at the same potentials (1.52 V and 1.40 V, respectively), observed when scanning is carried out in a solution containing both compounds.

The ratio of *E* vs. log *v* for B (Figure S4C), T (Figure S5C) and X (Figure S6C), shows a slight shift of *E* to more positive values as the scan rate increases,

which suggests the irreversibility of the reaction in the electrode for all compounds. The relationship between *E* vs. log *v* can be expressed by the Laviron equation [66], when the sweep rate is greater than 0.20 Vs<sup>-1</sup>, according to the following Eq. 2:

$$E = E^0 + 2.303RT/anF[\log(RTk_0/anF) - \log v] \quad (2)$$

Where '*α*' is the charge transfer coefficient for the molecule oxidation, '*k<sub>0</sub>*' is the standard heterogeneous rate constant of the reaction (s<sup>-1</sup>), '*v*' is the scan rate (V s<sup>-1</sup>), '*E<sup>0</sup>*' is the formal redox potential (V), '*T*' is the temperature (K), '*R*' is the universal gas constant (8.314 J K<sup>-1</sup> mol<sup>-1</sup>), '*n*' is the number of electrons involved in the rate determining step, and '*F*' is Faraday's constant (96485 C mol<sup>-1</sup>).

According to the experiments carried out, the relationship between the oxidation potentials and log *v* (0.20 Vs<sup>-1</sup>–0.50 Vs<sup>-1</sup>) for BTX can be given by the equations below. B: *E* = 0.05 log *v* + 1.8, *R*<sup>2</sup> = 0.996, T: *E* = 0.1 log *v* - 1.7, *R*<sup>2</sup> = 0.996, and X: *E* = 0.1 log *v* + 1.6, *R*<sup>2</sup> = 0.998.

Thus, '*αn*' values were calculated from the slope of these equations, for B (1.1), T (0.6) and X (0.6). As reported by Bard, Faulkner and White [67] the theoretical value of '*α*' for an irreversible process is 0.50, so the calculated values of '*n*' for B, T and X were 2.2, 1.2 and 1.2, respectively. The results found for '*n*' indicates that two electrons were involved in the B oxidation process, and one electron in the oxidation of T and X.

The value of '*k<sub>0</sub>*' was also calculated to inform about the speed of the electron transfer process involved in the oxidation of B on the electrode surface. For this, the Eq. 10 was used. The *E<sup>0</sup>* value was obtained using *E* vs. *v* for B (Figure S4D), T (Figure S5D) and X (Figure S6D). Considering the linear regression intercepts for B (*E* = 0.06 *v* + 1.8), T (*E* = 0.2 *v* + 1.4) and X (*E* = 0.1 *v* + 1.5), and *v* = 0, *E<sup>0</sup>* values were obtained as being 1.8 V, 1.4 V and 1.5 V vs. Ag/AgCl, for BTX, respectively. Thus, it was possible to obtain the following values for *k<sub>0</sub>* at 298 K 62.6 s<sup>-1</sup>, 68.2 s<sup>-1</sup> and 25.8 s<sup>-1</sup>, for B, T and X, respectively.

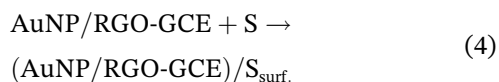
The surface concentration of BTX in AuNP/RGO-GCE was calculated using Eq. (3) [68].

$$I_p = n^2 F^2 A \Gamma v / 4RT \quad (3)$$

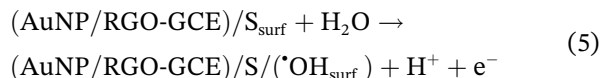
In this equation, '*A*' is the active surface area of the sensor in cm<sup>2</sup>, '*v*' is the scan rate, '*n*' is the number of electrons, '*I<sub>p</sub>*' is the respective peak current, and '*Γ*' is a surface concentration in mol cm<sup>-2</sup>. The '*Γ*' found values for BTX were 5.8 nmol cm<sup>-2</sup>, 3.9 nmol cm<sup>-2</sup> and 3.1 nmol cm<sup>-2</sup>, respectively.

Considering the found in the literature [47–51, 63], what was discussed above, and the characteristics of the electrode material [39] used in the present work, we propose the following detailed description of the oxidation reaction mechanism for the studied aromatics (BTX), as below:

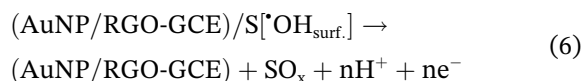
Firstly, each substrate, “S” (BTX) is adsorbed on the electrode surface (surf.).



When a potential above 1.3 V is reached, the discharge of water occurs in available active sites on the electrode surface “(AuNP/RGO-GCE)/S”, with the formation of hydroxyl free radicals ( $\bullet\text{OH}$ ) that remain physically adsorbed on the electrode surface, according to Eq. 5, below:



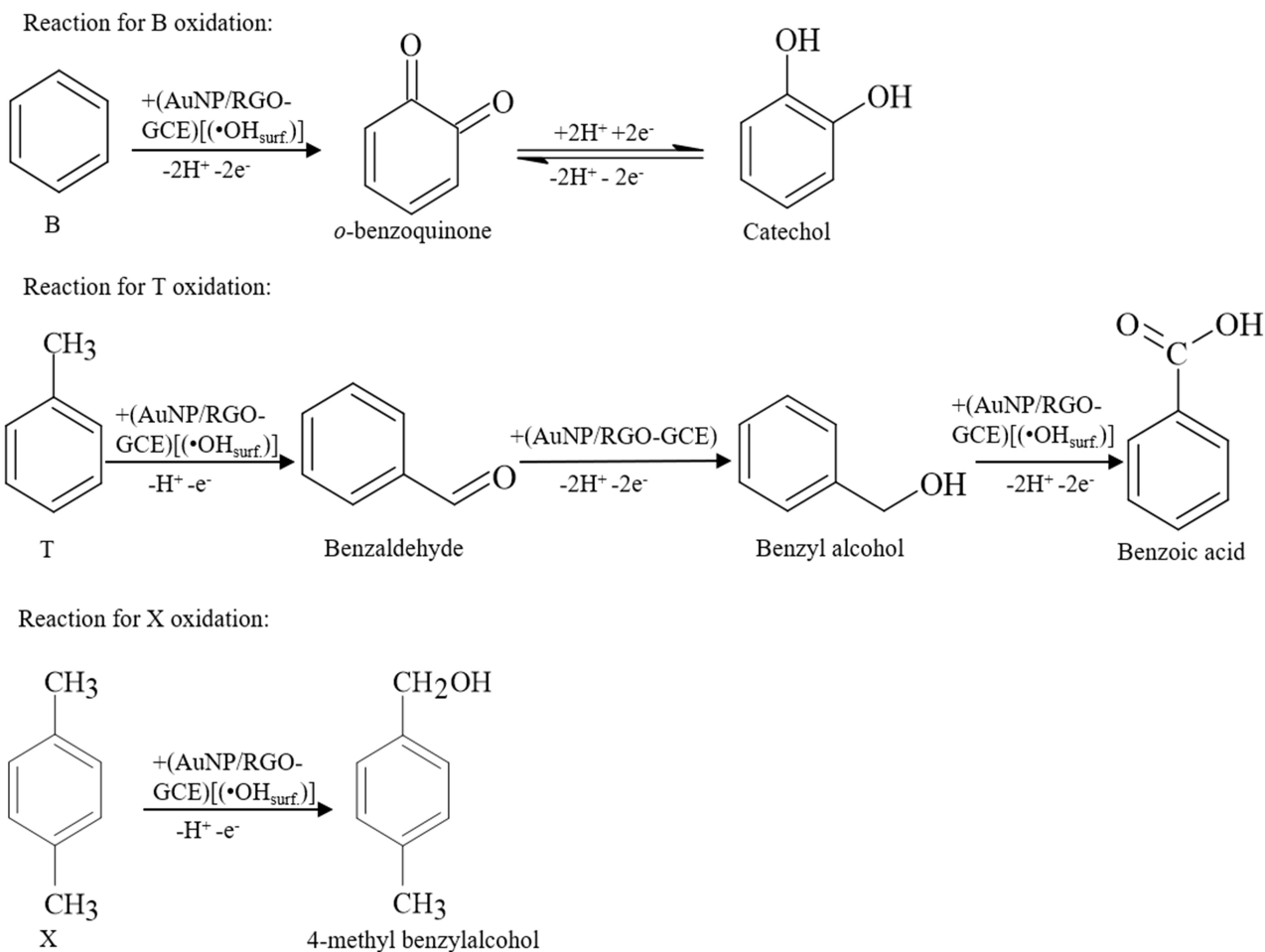
In the next step, the organic molecules (S), on the electrode surface, react with highly reactive oxidizing species ( $\bullet\text{OH}_{\text{surf.}}$ ), on the electrode surface, according to the Eq. 6, regenerating the electrode and generating oxidized by-products ( $\text{SO}_x$ ).



Considering all discussion above, and the number of electrons calculated for BTX ( $n=2$  for B, and 1 for T and X), the specific oxidation reactions for the three aromatics (BTX) are presented in Scheme 1.

### 3.3 | Possibility of simultaneous determination of BTX

To evaluate the possibility of simultaneous determination of BTX, tests were performed using voltametric techniques. CV (Figure S7A) and DPV (Figure S7B) with



Scheme 1 BTX oxidation mechanism.

concentration of BTX of 1.0 mM for CV and 200  $\mu\text{M}$  for DPV in  $\text{H}_2\text{SO}_4$  0.50 M solution. Both techniques allowed the identification of characteristic peaks for each analyte. Through VPD, it was possible to obtain a clearer position of the peaks for each analyte: B (1.7 V), T (1.5 V), and X (1.4 V). This result clearly proves the possibility of simultaneously determining the analytes. In order to obtain the best conditions to concurrently quantify BTX, the effect of the support electrolyte concentration ( $\text{H}_2\text{SO}_4$ ) was evaluated in the 0.1 M - 1.0 M concentration range, through peak currents comparison for BTX. DPV profiles (Figure S8) in the presence of BTX, showed that the best response in terms of peak current was obtained at the concentration of 0.50 M of  $\text{H}_2\text{SO}_4$ , with an average difference of current of 0.50  $\mu\text{A}$  in relation to the concentration of 0.1 M and 0.2  $\mu\text{A}$  in relation to the concentration of 1.0 M. DPV voltammograms in 0.50 M  $\text{H}_2\text{SO}_4$  showed good peak potential separation, approximately 0.11 V between X and T and 0.20 V from T to B. The observed peak separation clearly allows simultaneous determination of these compounds [23].

### 3.4 | Analytical performance

The DPV technique was used to determine the BTX with the AuNP/RGO-GCE sensor, and using the previously optimized parameters it was possible to build the analytical curves for BTX, determining each analyte individually or simultaneously. Individual measurements took place in two ways: firstly, the analytical curve was obtained for each analyte BTX separately, varying the concentration from 20  $\mu\text{M}$  to 160  $\mu\text{M}$ , as can be seen in Figure S9. Subsequently, the analytes were determined by changing the concentrations of

one analyte, while the other two were kept constant (100  $\mu\text{M}$ ) as shown in Figure 4. Analyzing the curves obtained, it was observed that the respective curves showed good linearity for B, T and X in the 30  $\mu\text{M}$ –240  $\mu\text{M}$  concentration range. It is possible to visualize in Figure 4 that the peak potentials of the three analytes were well separated by the AuNP/RGO-GCE sensor and the anodic peak current of each species was directly proportional to their concentrations. These results demonstrated that increasing the concentration of an analyte does not significantly influence the detection of the other two compounds. Values in details of the analytical curves, such as equations of the straight line, limit of detection (LOD) and limit of quantification (LOQ), can be seen more clearly in Table 1.

In Figure 5 it can be seen the DPV response with AuNP/RGO-GCE in the simultaneous determination of BTX in the concentration range of 30  $\mu\text{M}$  to 240  $\mu\text{M}$ . Figure 5A shows the three well-defined anodic peaks, with the peak currents of all analytes increasing proportionally to their concentrations. The excellent linear relationship between peak current ( $I_p$ ) values and concentrations is shown in Figure 5B–D, and the three clearly visible peaks indicate that the AuNP/RGO-GCE can be used for the simultaneous and accurate detection of the three analytes, showing that the response of one analyte does not significantly interfere with the determination of the others. The values referring to the analytical performance, including linear range of the equation, limit of detection (LOD) and limit of quantification (LOQ) for the individual and simultaneous detections of BTX using the proposed method are summarized in Table 1. The values obtained for LOD and LOQ are within the acceptable

TABLE 1 The analytical performance for individual and simultaneous determinations of BTX by DPV with the AuNP/RGO-GCE.

| Analyte        | Linear range ( $\mu\text{M}$ ) | Linear equation                             | $R^2$ | LOD ( $\mu\text{M}$ ) | LOQ ( $\mu\text{M}$ ) |
|----------------|--------------------------------|---|-------|-----------------------|-----------------------|
| B <sup>a</sup> | 20–160                         | $I = 0.015[\text{B}] - 2.5 \times 10^{-7}$  | 0.999 | 1.8                   | 6.2                   |
| T <sup>a</sup> |                                | $I = 0.012[\text{T}] - 1.2 \times 10^{-7}$  | 0.998 | 2.2                   | 7.2                   |
| X <sup>a</sup> |                                | $I = 0.014[\text{X}] - 2.3 \times 10^{-7}$  | 0.997 | 2.0                   | 6.6                   |
| B <sup>b</sup> | 30–240                         | $I = 0.013[\text{B}] - 3.4 \times 10^{-7}$  | 0.998 | 2.1                   | 7.2                   |
| T <sup>b</sup> |                                | $I = 0.011[\text{T}] - 2.1 \times 10^{-7}$  | 0.997 | 2.3                   | 7.7                   |
| X <sup>b</sup> |                                | $I = 0.010[\text{X}] - 2.8 \times 10^{-7}$  | 0.995 | 2.2                   | 7.5                   |
| B <sup>c</sup> | 30–240                         | $I = 0.0075[\text{B}] - 1.8 \times 10^{-7}$ | 0.999 | 2.2                   | 7.3                   |
| T <sup>c</sup> |                                | $I = 0.0052[\text{T}] - 8.3 \times 10^{-8}$ | 0.998 | 2.7                   | 8.9                   |
| X <sup>c</sup> |                                | $I = 0.0048[\text{X}] - 1.2 \times 10^{-7}$ | 0.997 | 2.6                   | 8.8                   |

<sup>a</sup> Individual analysis.

<sup>b</sup> Analysis of each analyte in the presence of the two others.

<sup>c</sup> Simultaneous analysis.

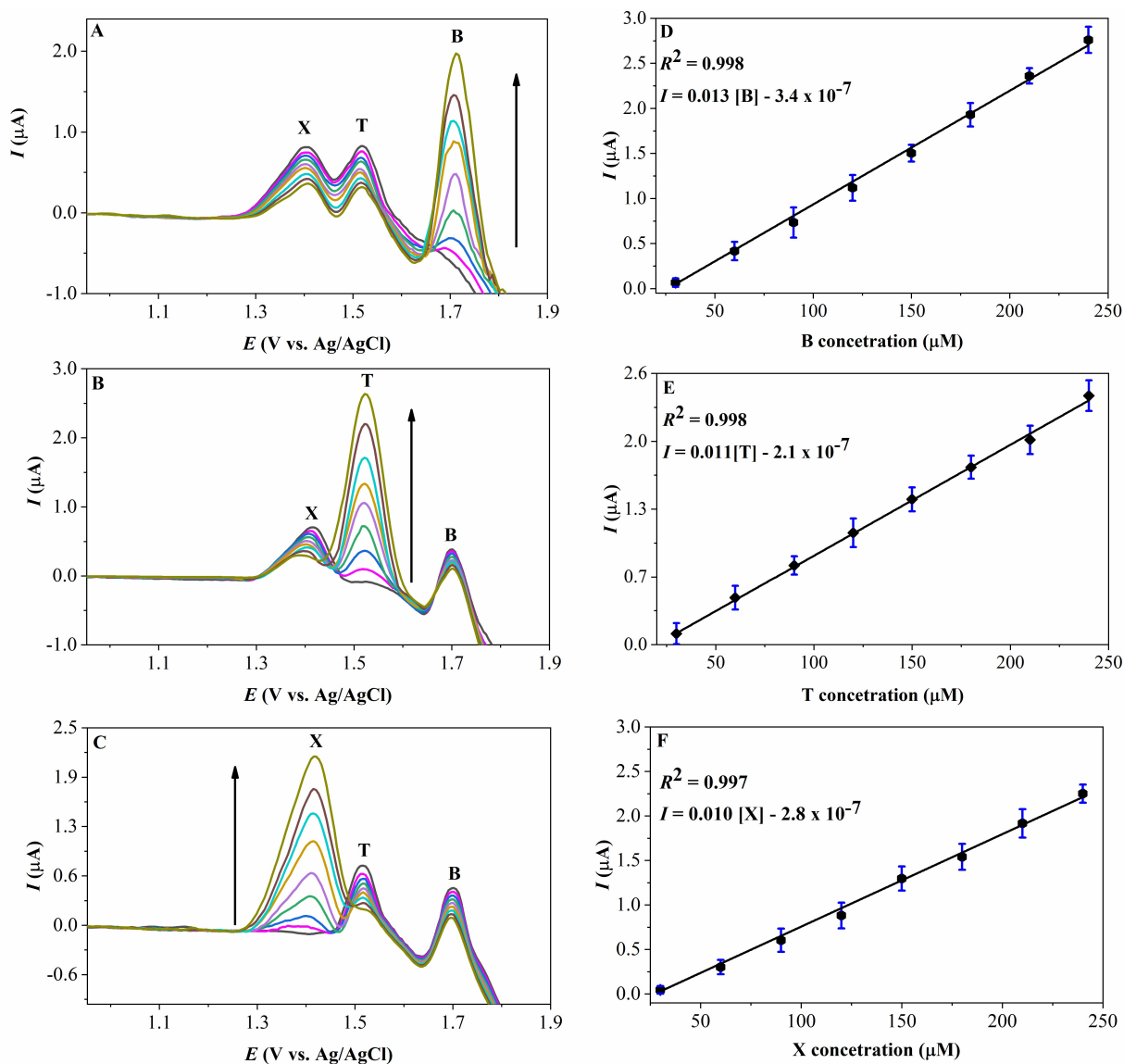


**FIGURE 4** AuNP/RGO-GCE DPV sensor in  $\text{H}_2\text{SO}_4$  (0.5 M), (A) 100  $\mu\text{M}$  of each of T and X, B in the concentration range of 30 to 240  $\mu\text{M}$ . (B) 100  $\mu\text{M}$  of each of B and X, T ranging in concentration from 30 to 240  $\mu\text{M}$ . (C) 100  $\mu\text{M}$  of each of B and T, X varying the concentration from 30 to 240  $\mu\text{M}$ . The linear relationship between peak current ( $I$ ) and concentrations of (D) B, (E) T, and (F) X.

**TABLE 2** Comparison of different modified electrodes for BTX determination.

| Electrode        | Technique | Linear range ( $\mu\text{M}$ ) |        |        | LOD ( $\mu\text{M}$ ) |     |     | References |
|------------------|-----------|--------------------------------|--------|--------|-----------------------|-----|-----|------------|
|                  |           | B                              | T      | X      | B                     | T   | X   |            |
| BDD <sup>a</sup> | SWV       | 20–200                         | 20–200 | 20–200 | 0.3                   | 0.8 | 0.9 | [23]       |
| AuNP/RGO-GCE     | DPV       | 30–240                         | 30–240 | 30–240 | 2.2                   | 2.7 | 2.6 | This work  |

range for BTX determination, according to the legislation for the treatment of industrial waste effluents [6–10].

The comparison of the AuNP/RGO-GCE sensor with similar ones reported in the literature is shown in Table 2. The data in this table shows that in

comparison with previous literature, AuNP/RGO-GCE can simultaneously detect B, T and X with sensitivity similar to that of the literature with low detection limits. It is important to mention and take into account that from the electrochemical point of view, only the work using the boron-doped diamond

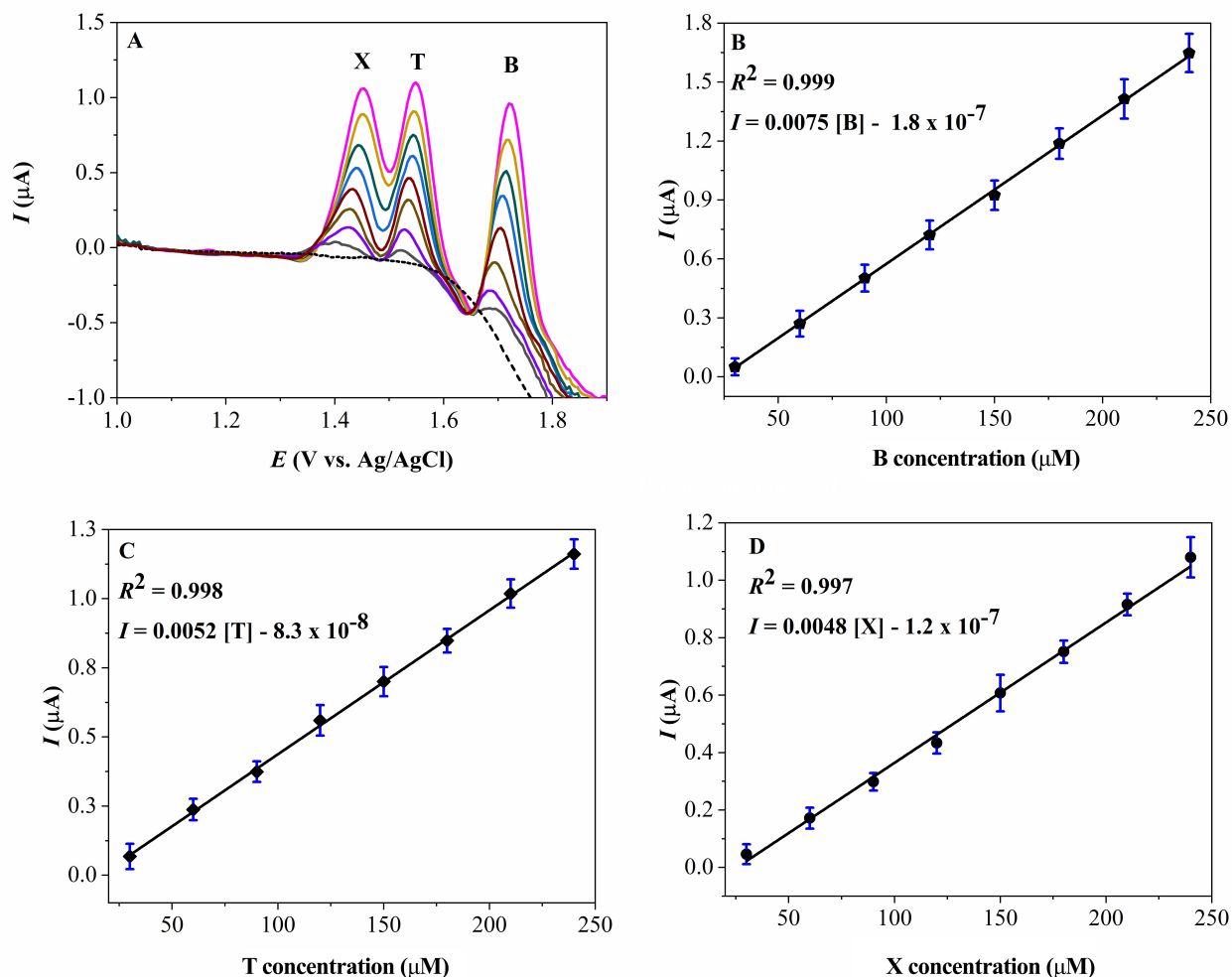


FIGURE 5 (A) DPV curves of AuNP/RGO-GCE in  $\text{H}_2\text{SO}_4$  (0.50 M), containing 30  $\mu\text{M}$ –240  $\mu\text{M}$  BTX; linear relationship between peak current ( $I_p$ ) and concentrations of (B) B, (C) T, and (D) X.

TABLE 3 Determination of BTX in a water sample from the fuel station separator box.

| Analyte | Add ( $\mu\text{M}$ ) | Found ( $\mu\text{M}$ ) | Recovery (%) | RSD (%) |
|---------|-----------------------|-------------------------|--------------|---------|
| B       | –                     | $63.5 \pm 2.1$          | –            | –       |
|         | 80                    | $145.5 \pm 1.9$         | 102.5        | 2.5     |
|         | 120                   | $185.5 \pm 1.8$         | 101.6        | 1.9     |
|         | 160                   | $221.7 \pm 2.3$         | 98.8         | 2.0     |
| T       | –                     | $83.4 \pm 2.0$          | –            | –       |
|         | 80                    | $162.2 \pm 2.1$         | 98.5         | 3.8     |
|         | 120                   | $205.5 \pm 1.7$         | 101.7        | 2.2     |
|         | 160                   | $247.3 \pm 2.1$         | 102.4        | 1.4     |
| X       | –                     | $79.7 \pm 1.0$          | –            | –       |
|         | 80                    | $157.9 \pm 1.2$         | 97.8         | 2.1     |
|         | 120                   | $202.1 \pm 1.0$         | 102.0        | 2.2     |
|         | 160                   | $244.7 \pm 1.2$         | 103.1        | 1.8     |

electrode for simultaneous determination of BTX was found.

### 3.5 | Reproducibility and repeatability, stability and selectivity of AuNP/RGO-GCE

The reproducibility, repeatability and stability of AuNP/RGO-GCE were investigated in H<sub>2</sub>SO<sub>4</sub> (0.50 M) containing 150 μM BTX using the DPV technique. The sensor reproducibility was investigated using six different sensors (1 to 6) prepared independently under the same conditions as showed in Figure S10A. The relative standard deviations (RSD) obtained were: 2.8% for B, 3.3% for T, and 3.1% for X. The repeatability was evaluated 10 successive times with the same modified electrode (Figure S10B). The RSD obtained for the analytes were: 1.5% for B, 2.4% for T, and 2.6% for X. The sensor stability was measured after sensor storage for 30 days at an ambient temperature of 25 °C (Figure S10C). The results showed that the sensor still presented for 90.8% for B, 91.2% for T, and 92.2% for X of their initial currents after this period, demonstrating that, in fact, the sensor presents good stability. The results clearly indicate that AuNP/RGO-GCE has good repeatability, reproducibility and stability, suggesting that the proposed method is suitable for the simultaneous determination of BTX.

The interference evaluation for the sensor AuNP/RGO-GCE was evaluated in the presence of possible interfering compounds, such as: catechol, *p*-benzoquinone, resorcinol, ethanol, pyrene, ions of K<sup>+</sup>, Mg<sup>2+</sup> and Pb<sup>2+</sup>. The study was carried out using a BTX concentration of 1.50 μM, in H<sub>2</sub>SO<sub>4</sub> 0.50 M, and ratios of 1:1 and 1:10 of analyte: possible interferent. The results obtained in the presence of these compounds showed relative standard deviation values ranging from 0.6% to 5.1%, as can be seen in Table S1. Based on these results, it can be concluded that the proposed method using DPV did not present significant interference for the detection of BTX in the presence of these possible interferents.

### 3.6 | Real sample analysis

To verify the performance and applicability of the procedure, the electrochemical sensor was applied to the determination of BTX in wastewater samples, from the separator box of gas stations, using the standard addition method to determine the concentration of BTX, as shown in Figure S11A. Standard aliquots of BTX were added in the concentration range of 80 μM to 160 μM. Through Figure S11 B, C, and D the following equations were obtained:  $I_p = 0.0034 [X] + 3.0 \times 10^{-7}$ ;  $I_p = 0.0022$

$[T] + 1.8 \times 10^{-7}$ ,  $I_p = 0.0026 [B] + 1.7 \times 10^{-7}$ , for X, T and B, respectively. According to the results presented, it was possible to find BTX in the studied samples, obtaining through the extrapolation of the straight lines obtained (Figure S11B, C, D) the concentrations of 130.8 μM, 163.6 μM and 176.4 μM for B, T and X, respectively. It was considered the dilution process described in the topic "Real sample preparation and quantification method". The values found for BTX are about 8.5, 12.5, and 11.7 times higher than the values established by Brazilian legislation (CONAMA Resolution number 430/2011 [6]) for B, T, and X, respectively. These results indicate a necessary treatment of the analyzed effluents so that the water is within the quality standards established by the resolution. The results regarding the recovery study are summarized in Table 3, showing a variation from 97.8% to 103.1%, which indicates that the method has a relatively good degree of accuracy, and the proposed sensor can be applied successfully to determine BTX in industrial wastewater samples.

## 4 | CONCLUSION

The present work reported the development of AuNP/RGO-GCE sensor based on reduced graphene oxide combined with gold nanoparticles. The modified electrode was successfully characterized by cyclic voltammetry (CV), electrochemical impedance spectroscopy (EIS) and scanning electron microscope (SEM), and the data obtained showed that the AuNP were efficiently synthesized on the RGO-GCE surface. The electrode modification plays a key role in improving the sensor performance, which can be attributed to the increase in the conductive surface area of the material, thus favoring the electron transfer process and the consequent increased anodic peak current and high conductivity caused by the application of AuNP on the RGO-GCE. The suitable properties of the proposed sensor enabled its application toward the simultaneous determination of BTX in wastewater samples using the DPV technique. Considering criteria such as simplicity of handling, low cost, good reproducibility, repeatability and low influence of the possible interferent studied, the proposed electrochemical sensor is presented as a viable alternative for the simultaneous determination of BTX in real water samples.

### ACKNOWLEDGMENTS

The authors are grateful to CAPES-PROCAD AM [Edital PROCAD AMAZÔNIA 2018 - Line 2; Number SCBA: 88887.200615/2018-00], CNPq [PQ 2017, Proc. 310664/2017-9], FAPEMA [Proc. Edital UNIVERSAL-01136/17],

ANP [Contract PMQC N° 1.028/2021; Research Project QUALIPETRO CONSEPE-UFMA N° 2.460/22], and FA-PESP [grant 2018/12131-6 and 2017/22401-8] for the financial support and fellowships received, granted in the course of this research.

### CONFLICT OF INTEREST STATEMENT

There are no conflicts to declare.

### DATA AVAILABILITY STATEMENT

The data that support the findings of this study are available from the corresponding author upon reasonable request.

### ORCID

Edmar Pereira Marques  <http://orcid.org/0000-0002-5685-7869>

### REFERENCES

1. B. Yu, Z. Yuan, Z. Yu, F. Xue-song, *Chem. Eng. J.* **2022**, 435, 134825.
2. I. G. S. da Silva, F. C. G. de Almeida, N. M. P. R. Silva, A. A. Casazza, A. Converti, L. A. Sarubbo, *Energies*. **2020**, 13, 4664.
3. K. Salama, E. Omar, M. Zafar, *Indian J. Occup. Environ. Med.* **2020**, 24, 163.
4. M. Dehghani, A. Mohammadpour, A. Abbasi, I. Rostami, E. Gharehchahi, Z. Derakhshan, M. Ferrante, G. O. Conti, *Environ. Res.* **2022**, 204, 112155.
5. K. M. G. Lima, I. M. Raimundo, M. F. Pimentel, *Sens. Actuators B* **2011**, 160, 691–697.
6. CONAMA, Ministério do Meio Ambiente Conselho Nacional do Meio Ambiente, [http://conama.mma.gov.br/?option=com\\_sisconama&task=arquivo.download&id=627](http://conama.mma.gov.br/?option=com_sisconama&task=arquivo.download&id=627).
7. CONAMA, Ministério do Meio Ambiente Conselho Nacional do Meio Ambiente, [http://conama.mma.gov.br/?option=com\\_sisconama&task=arquivo.download&id=530](http://conama.mma.gov.br/?option=com_sisconama&task=arquivo.download&id=530).
8. A. R. P. da Motta, C. P. Borges, A. Kiperstok, K. P. Esquerre, P. M. Araujo, L. da P N Branco, *Eng. Sanit. e Ambient.* **2013**, 18, 15–26.
9. M. Stewart, K. Arnold, *Produced Water Treatment Field Manual*, Gulf Professional Publishing, Massachusetts, **2011**.
10. A. C. Klemz, S. E. Weschenfelder, S. L. C. Neto, M. S. P. Damas, J. C. T. Viviani, L. P. Mazur, B. A. Marinho, L. S. Pereira, A. Silva, J. A. B. Valle, A. A. U. Souza, S. M. A. Selene, *J. Pet. Sci. Eng.* **2021**, 199, 108282.
11. K. Dalvand, A. Ghiasvand, *Anal. Chim. Acta.* **2019**, 1083, 119–129.
12. M. Karlowatz, M. Kraft, B. Mizaikoff, *Anal. Chem.* **2004**, 76, 2643–2648.
13. P. Noor, M. Khanmohammadi, B. Roozbehani, A. Bagheri Garmarudi, *Monatsh. Chem.* **2018**, 149, 1341–1347.
14. H. S. Jung, E. H. Koh, C. W. Mun, J. Min, W. Sohng, H. Chung, J. Y. Yang, S. Lee, H. J. Kim, S. G. Park, M. Y. Lee, D. H. Kim, *J. Mater. Chem. C* **2019**, 7, 13059–13069.
15. S. Panneer Selvam, K. Yun, *Sens. Actuators B* **2020**, 302, 127161.
16. C. Gu, X. Xu, J. Huang, W. Wang, Y. Sun, J. Liu, *Sens. Actuators B. Chem.* **2012**, 174, 31–38.
17. H. Ma, Y. Xu, Z. Rong, X. Cheng, S. Gao, X. Zhang, H. Zhao, L. Huo, *Sens. Actuators B* **2012**, 174, 325–331.
18. X. Gao, H. Zhao, J. Wang, X. Su, F. Xiao, *Ceram. Int.* **2013**, 39, 8629–8632.
19. F. Chávez, G. F. Pérez-Sánchez, O. Goiz, P. Zaca-Morán, R. Peña-Sierra, A. Morales-Acevedo, C. Felipe, M. Soledad-Priego, *Appl. Surf. Sci.* **2013**, 275, 28–35.
20. M. H. Seo, M. Yuasa, T. Kida, J. S. Huh, N. Yamazoe, K. Shimano, *Sens. Actuators B* **2011**, 154, 251–256.
21. C. Sun, X. Su, F. Xiao, C. Niu, J. Wang, *Sens. Actuators B* **2011**, 157, 681–685.
22. P. Nagaraju, Y. Vijayakumar, G. L. N. Reddy, M. V. Ramana Reddy, *J. Mater. Electron.* **2018**, 29, 11457–11465.
23. G. G. F. Junior, T. M. Florêncio, R. J. Mendonça, G. R. Salazar-Banda, R. T. S. Oliveira, *Electroanalysis*. **2019**, 31, 554–559.
24. K. Beaver, A. Dantanarayana, S. D. Minter, *J. Phys. Chem. B.* **2021**, 125, 11820–11834.
25. M. Mehmandoust, S. Çakar, M. Özacar, S. Salmanpour, N. Erk, *Top. Catal.* **2023**, 65, 564–576.
26. T. Iftikhar, M. Asif, A. Aziz, G. Ashraf, S. Jun, G. Li, H. Liu, *Trends Environ. Anal. Chem.* **2021**, 31, e00138.
27. B. Mostafiz, S. A. Bigdeli, K. Banan, H. Afsharara, D. Hatamabadi, P. Mousavi, C. M. Hussain, R. Keçili, F. Ghorbani-Bidkorbeh, *Trends Environ. Anal. Chem.* **2021**, 32, e00144.
28. F. Zhang, K. Yang, G. Liu, Y. Chen, M. Wang, S. Li, R. Li, *Composites Part A* **2022**, 160, 107051.
29. S. Erdoğan Kablan, A. Yılmaz, Ü. Kervan, N. Özalıtın, E. Nemutlu, *Talanta*. **2023**, 253, 124005.
30. L. Zhang, M. Yin, X. Wei, Y. Sun, Y. Chen, S. Qi, X. Tian, J. Qiu, D. Xu, *Diamond Relat. Mater.* **2022**, 128, 109311.
31. H. Lu, S. Sha, S. Yang, J. Wu, J. Ma, C. Hou, Z. Sheng, *Appl. Surf. Sci.* **2021**, 538, 147948.
32. D. Karačić, S. J. Gutic, B. Vasic, V. M. Mirsky, N. V. Skorodumova, S. V. Mentus, I. A. Pašti, *Electrochim. Acta.* **2022**, 410, 140046.
33. R. Zhao, X. Xu, L. Hu, *ACS Appl. Polym. Mater.* **2021**, 3, 5155–5161.
34. S. J. Malode, K. Prabhu, B. G. Pollet, S. S. Kalanur, N. P. Shetti, *Electrochim. Acta.* **2022**, 429, 141010.
35. A. C. Mendes Hacke, D. Lima, S. Kuss, *J. Electroanal. Chem.* **2022**, 922, 116786.
36. S. Chen, Y. Xie, X. Guo, D. Sun, *Microchem. J.* **2022**, 181, 107715.
37. K. Dhara, R. M. Debiprosad, *Anal. Biochem.* **2019**, 586, 113415.
38. X. Zhao, Z. Guo, Y. Hou, L. Gbologah, S. Qiu, X. Zeng, R. Cao, J. Zhang, *Chem. Pap.* **2022**, 76, 3679–3690.
39. M. A. Beluomini, J. L. da Silva, G. C. Sedenho, N. R. Stradiotto, *Talanta*. **2017**, 165, 231–239.
40. M. A. Beluomini, J. L. Silva, N. R. Stradiotto, *Microchim. Acta.* **2018**, 185, 170.
41. J. Mocak, A. M. Bond, S. Mitchell, G. Scollary, A. M. Bond, *Pure Appl. Chem.* **1997**, 69, 297–328.
42. D. T. Burns, K. Danzer, A. Townshend, *Pure Appl. Chem.* **2003**, 74, 2201–2205.
43. H. Ibrahim, Y. Temerk, *Sens. Actuators B* **2021**, 347, 130626.
44. H. Ibrahim, Y. Temerk, *J. Electroanal. Chem.* **2020**, 859, 113836.

45. T. M. Mariano, M. A. Beluomini, N. R. Stradiotto, *J. Braz. Chem. Soc.* **2021**, *32*, 249–259.
46. Y. Guo, L. Feng, *Front. Chem.* **2022**, *10*, 898924.
47. R. T. S. Oliveira, G. R. Salazar-Banda, M. C. Santos, M. L. Calegario, D. W. Miwa, S. A. S. Machado, L. A. Avaca, *Chemosphere.* **2007**, *66*, 2152–2158.
48. K.-W. Kim, M. Kuppaswamy, R. F. Savinell, *J. Appl. Electrochem.* **2000**, *30*, 543–549.
49. B. Seo, W. H. Lee, Y. J. Sa, U. Lee, H. S. Oh, H. Lee, *Appl. Surf. Sci.* **2020**, *534*, 147517.
50. R. Tomat, A. Rigo, *J. Appl. Electrochem.* **1984**, *14*, 1–8.
51. P. Loyson, S. Gouws, B. Barton, M. Ackermann, *S. Afr. J. Chem.* **2004**, *57*, 53–56.
52. R. B. S. Sawczuk, H. A. Pinheiro, J. N. R. Santos, I. C. B. Alves, H. D. C. Viegas, C. A. Lacerda, J. C. K. Sousa, E. P. Marques, A. L. B. Marques, *Int. J. Environ. Anal. Chem.* **2021**, *103*, 1733–1750.
53. A. R. L. Silva, A. J. Santos, C. A. Martínez-Huitle, *RSC Adv.* **2018**, *8*, 3483–3492.
54. F. Montilla, F. Huerta, E. Morallon, J. L. Vazquez, *Electrochim. Acta.* **2000**, *45*, 4271–4277.
55. B. Lee, H. Naito, T. Hibino, *Angew. Chem.* **2012**, *124*, 455–459.
56. I. Cesarino, F. C. Moraes, T. C. R. Ferreira, M. R. V. Lanza, S. A. S. Machado, *J. Electroanal. Chem.* **2012**, *672*, 34–39.
57. M. M. Rahman, *Mater. Chem. Phys.* **2020**, *245*, 122788.
58. M. Balaganesh, S. Lawrence, C. Christopher, A. J. Bosco, K. Kulangiappar, K. J. S. Raj, *Electrochim. Acta.* **2013**, *111*, 384–389.
59. A. J. Bard, L. R. Faulkner, *Electrochemical Methods: Fundamentals and Applications*, 2 ed., John Wiley & Sons, New York, **2001**.
60. M. A. Beluomini, N. R. Stradiotto, M. V. Boldrin, *Food Chem.* **2021**, *353*, 129427.
61. N. P. Shetti, D. S. Nayak, G. T. Kuchinad, R. R. Naik, *Electrochim. Acta.* **2018**, *269*, 204–211.
62. F. Montilla, E. Morallón, J. L. Vázquez, *Electrochim. Acta.* **2002**, *47*, 4399–4406.
63. F. Su, C. Lu, S. Hu, *Colloids Surf. A Physicochem. Eng. Asp.* **2010**, *353*, 83–91.
64. S. Rodsud, W. Limbut, *J. Electrochem. Soc.* **2019**, *166*, B771–B779.
65. K. Saisahas, A. Soleh, K. Promsuwan, A. Phonchai, N. S. M. Sadiq, W. K. Teoh, K. H. Chang, A. F. L. Abdullah, W. Limbut, *J. Pharm. Biomed. Anal.* **2021**, *198*, 113958.
66. E. Laviron, *J. Electroanal. Chem. Interfacial Electrochem.* **1979**, *101*, 19–28.
67. A. J. Bard, L. R. Faulkner, H. S. White, *Electrochemical Methods: Fundamentals and Applications*, 1 ed., John Wiley & Sons, Oxford, **2022**.
68. M. M. Shanbhag, N. P. Shetti, S. J. Malode, R. S. Veerapur, K. R. Reddy, *FlatChem.* **2021**, *28*, 100255.

## SUPPORTING INFORMATION

Additional supporting information can be found online in the Supporting Information section at the end of this article.

**How to cite this article:** I. Carlos Braga Alves, J. Ribamar Nascimento dos Santos, E. Pereira Marques, L. Carvalho Martiniano de Azevedo, M. Azevedo Beluomini, N. Ramos Stradiotto, A. Lopes Brandes Marques, *Electroanalysis* **2023**, *35*, e202300260. <https://doi.org/10.1002/elan.202300260>

# Graphical Abstract

The contents of this page will be used as part of the graphical abstract of html only.  
It will not be published as part of main.

